UNIVERSITY OF CLAUDE BERNARD LYON 1

Polytech Lyon

Estimation of Image-Derived Arterial Input Function in Brain PET Imaging:
Application to Modeling PET Dynamics of Glucose Metabolism in Patients with Impaired Consciousness

By SEPAND ALI MADAD SOLTANI

Master 2 in Medical Device Engineering
Internship Report

Supervised by INÉS MÉRIDA and NICOLAS COSTES
Academic Advisor: KEVIN TSE VE KOON

2024-2025

Abstract

Positron Emission Tomography (PET) combined with kinetic modeling enables quantitative assessment of physiological processes through the use of an arterial input function (AIF). Traditional AIF acquisition via arterial sampling is invasive and challenging, particularly in comatose patients. This study aimed to enhance a non-invasive Bayesian Geometric Transfer Matrix (BGTM) method for estimating image-derived input function (IDIF) using Time-of-Flight Magnetic Resonance Angiography (TOF-MRA) acquired simultaneously with dynamic PET on a hybrid PET/MR scanner. The proposed method integrates TOF-MRA-guided carotid segmentation with a Bayesian framework incorporating population-based AIF priors to address partial volume effects. Evaluated on a cohort of 56 comatose patients, the refined segmentation pipeline, incorporating a cuboid mask to exclude non-carotid tissues, improved robustness in challenging cases. The BGTM approach demonstrated a 57% reduction in mean absolute error in the cumulative Area Under the Curve (cAUC) errors (14,202 vs. 33,764 vs, $p < 0.0001$) and a signifact reduction (14.1% vs. 33.0%, $p < 0.0001$) in mean absolute percentage error (MAPE) for glucose metabolic rate (MR_{glu}) quantification compared to conventional GTM method. However, high variability in MR_{glu} and cAUC errors(71% and 65% coefficient of variation, respectively) highlights inconsistencies in the method. These results position BGTM as a promising pathway toward reducing reliance on invasive arterial sampling, though addressing residual variability remains critical for future clinical applications.

Keywords: Dynamic FDG-PET, Image-Derived Input Function, Hybrid PET/MRI, Bayesian Framework

Contents

Introduction

1.1 Positron Emission Tomography

Positron Emission Tomography (PET) is an in vivo functional imaging technique widely used in clinical and research settings to monitor physiological and biochemical processes. In PET, a biologically active molecule is labeled with a positron-emitting radioisotope, serving as a radiotracer, and then injected into the body. As the radiotracer accumulates in target tissues, its radioactive decay produces positrons, which interact with electrons to emit pairs of gamma photons in nearly opposite directions. These photons are detected by the PET scanner, and image reconstruction algorithms generate a three-dimensional representation of the tracer distribution. This imaging modality allows for the investigation of metabolic changes, receptor binding, and other biochemical processes, providing invaluable information in oncology, neurology, cardiology, and other fields.

There are two main categories in PET image acquisition: static imaging and dynamic imaging. Static PET involves acquiring a single scan after the radiotracer injection. This single snapshot offers a powerful yet simplified view of tracer distribution. The common quantification metric in static imaging is the Standardized Uptake Value (SUV), which normalizes tissue uptake by the injected dose and weight of the subject, allowing for a semi-quantitative comparison of tracer accumulation across different tissues or over time [1]. Due to its simplicity, static PET is widely used in clinical settings; however, it also has limitations. Because it reflects only one time point, the SUV cannot capture the temporal dynamics of tracer uptake and clearance, and various physiological factors may influence its measurements, thereby reducing its accuracy.

Dynamic PET imaging provides a more comprehensive view of radiotracer kinetics by acquiring a series of images over a period ranging from a few minutes to more than an hour post-injection, depending on the tracer type. Instead of a single snapshot, dynamic imaging produces time-activity curves (TACs) that illustrate how tracer concentration in each tissue changes throughout the scanning period. This approach enables the measurement of physiological parameters such as the tracer rate of influx (K_i) for radiotracers with irreversible uptake (e.g. ^{18}F-FDG), volume of distribution (V_T), and the rates of phosphorylation and dephosphorylation.

1.2 Kinetic Modeling

To quantify pharmacokinetic parameters, kinetic modeling is employed. Compartmental modeling is the most popular and is considered the most accurate approach in kinetic modeling. In compartmental modeling, the distribution and kinetics of a radiotracer are described by dividing the system into distinct compartments, each representing a pool of tracer that behaves uniformly. Interactions between compartments can be unidirectional or bidirectional, meaning the tracer may either move in and out or only enter a compartment. Various graphical models (e.g., the Logan [2] and Patlak [3] methods), as well as classical compartmental model fitting approaches, are used to analyze tracer kinetics.

Figure 1.1 shows the two-tissue compartment model (2TCM), also known as the three-compartment model, in series mode. This model comprises one tissue compartment for the free tracer, $C_F(t)$, and another for the receptor-bound tracer, $C_B(t)$, in addition to an external compartment representing the tracer concentration in the plasma or blood, denoted as the input function $C_P(t)$.

The tracer kinetics are governed by a series of first-order differential equations, in which the exchange rates between the compartments are considered constant:

$$\frac{dC_F(t)}{dt} = K_1\,C_P(t)\; -\; \big(k_2 + k_3\big)C_F(t)\; +\; k_4 C_B(t)\,, \tag{1.1}$$

$$\frac{dC_B(t)}{dt} = k_3\,C_F(t)\; -\; k_4\,C_B(t), \tag{1.2}$$

where K_1, k_2, k_3, and k_4 are the constant rate parameters.

It is generally assumed that once ^{18}F-FDG is phosphorylated (i.e., bound), there is little to no dephosphorylation back to the free (unbound) compartment [4]. Therefore, we can set $k_4 = 0$, treating the process as irreversible. Thus, Equations (1.1) and (1.2) simplify to

$$\frac{dC_F(t)}{dt} = K_1\,C_P(t)\; -\; \big(k_2 + k_3\big)C_F(t)\,, \tag{1.3}$$

$$\frac{dC_B(t)}{dt} = k_3\,C_F(t)\,. \tag{1.4}$$

The total radiotracer tissular kinetic measured by PET (the PET data), $C_T(t)$, is given by

$$C_T(t)\; =\; C_F(t)\; +\; C_B(t)\; +\; C_P(t). \tag{1.5}$$
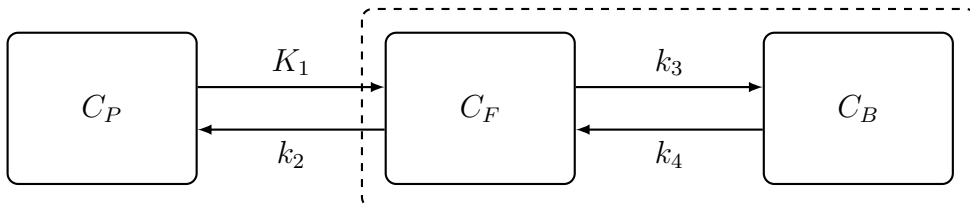
Figure 1.1: Schematic of the two-tissue compartment model (2TCM)

Thus to solve this system of equations and to estimate K_1, k_2, and k_3 parameters, we must fit the model using the measured PET TACs (C_T) and the input function (C_P). Consequently, the influx rate (trapping rate) of ^{18}F-FDG in the tissue, K_i, can be derived as

$$K_i = \frac{K_1 \times k_3}{k_2 + k_3} \, . \tag{1.6}$$

^{18}F-FDG is an analog of glucose, not glucose itself. To convert the ^{18}F-FDG trapping rate into the actual rate of glucose metabolism, both the glucose concentration and the lumped constant must be taken into account.

$$\text{MR}_{glu} \; (\text{µmol/min/100g}) = \frac{[C]}{LC} \cdot K_i \, . \tag{1.7}$$

Here, MR_{glu} represents the metabolic rate of glucose, $[C]$ denotes the glucose concentration, and LC is the lumped constant.

1.3   Input Function

1.3.1   Arterial Input Function

The arterial input function (AIF) is considered the gold standard for obtaining the input function. It is determined by inserting an arterial catheter into the patient and continuously drawing blood samples to measure the radiotracer concentration, thereby obtaining the blood activity curve used in the quantification model. However, this procedure is invasive and can cause discomfort, potentially discouraging patients from undergoing future examinations. Furthermore, this method is labor-intensive and requires trained personnel to manage both the patient and the measurement devices.

1.3.2   Image Derived Input Function

The image-derived input function (IDIF) has been proposed as a non-invasive alternative for obtaining the input function. IDIF techniques typically involve identifying vascular structures or regions with high blood pool activity within the imaging field and extracting the input function directly from the PET images. In brain PET imaging, the carotid arteries are the largest vessels present in the limited field of view (FOV) and have a diameter of approximately 5 mm, which is comparable to the typical spatial resolution of PET (4-6mm FWHM). Therefore, directly extracting the carotids from PET images is impractical due to the limited resolution and the strong partial volume effects (PVE) present.

With the emergence of hybrid PET/MRI machines, it has become feasible to acquire both functional and anatomical data simultaneously. MRI provides high-resolution soft tissue contrast, while PET captures metabolic activity. For instance, time-of-flight MR angiography (TOF-MRA) delivers excellent arterial contrast, which allows for accurate segmentation

of vascular structures such as the carotid arteries. However, even with a high-resolution anatomical guidance, directly applying the segmented arterial mask to the PET images introduces challenges [5]. In particular, the limited spatial resolution of PET can lead to partial volume effects, resulting in inaccuracies in the derived input function. Consequently, additional correction techniques are required to mitigate these effects and ensure reliable quantification.

Several methods have been developed to enhance IDIF accuracy by addressing partial volume correction and automation challenges. Early PET-only approaches primarily focused on classical partial volume correction (PVC) techniques [6], while more recent methods have explored supervised clustering algorithms [7] and deep learning approaches [8, 9]. Hybrid PET/MRI methods improve carotid artery delineation by leveraging anatomical imaging. The caliPER software, for instance, employs a semi-automated approach for IDIF extraction using carotid masks obtained from T1 or TOF-MRA images, incorporating partial volume correction [10]. Additionally, fully automated methods have been proposed to enhance carotid segmentation and PVC techniques [11, 12, 13, 14].

Irace et al. [15] proposed an automatique method for IDIF estimation by performing TOF-MRA driven carotid segmentation and using a Bayesian framework for incorporating prior knowledge into a geometric transfer matrix method [16]—a classical partial volume correction technique. In this work, the aim was to improve this method and enhance accuracy by evaluating it on a dataset of comatose patients.

Materials and Methods

2.1 Dataset Description

56 acute comatose patients were included in the study between 7 days and 30 days after the coma onset (46 ± 16 years old; 21 females). PET data were acquired in list mode during 90 min from the injection of an intravenous bolus of ^{18}F-FDG. Simultaneously, an arterial time-of-flight MR was acquired in axial orientation, with a voxel size of 0.3×0.3×0.7 mm. Raw PET data were rebinned into 24-time frames (variable length frames : 8×15 s, 3×60 s, 5×120 s, 1×300 s, 7×600 s) sinograms for dynamic reconstruction. Reconstruction yielded a voxel size of 1.04×1.04×2.08 mm^3 in a matrix of 344×344×127 voxels .

AIF in the whole blood and plasma were measured from 26 arterial blood samples manually collected (with the following timing: every 5 s for the first minute, every 15 s until second minute, and at times 3, 5, 10, 20, 30, 45, 60, 75, 80, 85 and 90 minutes post-injection) and counted with a gamma counter.

2.2 Carotid Segmentation

Figure 2.1 shows the complete pipeline for the carotid segmentation. Since vessels appear as hypersignal in TOF-MRA, a high-intensity thresholding technique was employed (Step II). First, a threshold value was computed by selecting all nonzero intensity values and then determining the intensity level at the (1 - 0.003) quantile (i.e., the 99.7th percentile) of these intensities. Only voxels exceeding this threshold and located outside the brain mask were retained. Next, a region-growing step (Step III) was applied to refine the initial selection, ensuring that continuous vascular structures were captured as the final carotid mask [15].

In addition to arteries, venous structures and possible brain lesions may also appear as hypersignal and might be selected by the algorithm. To exclude them, a cuboid mask was defined in a reference image covering the neck area up to the bottom of the brain, where the carotid artery is most likely to appear (Step I). The reference image used was the standard MNI152 atlas, which was registered to one of the subject's TOF-MRA images. This registration artificially increased the FOV—effectively achieved by zero-padding the matrix—to include the neck region. The TOF-MRA image was then registered to the reference image using an affine registration technique (FSL FLIRT) [17]. Using the obtained affine

matrix, the cuboid mask was first transformed and then applied to the TOF-MRA image before thresholding (Step II) to ensure the mentioned unwanted tissues will not affect the intensity histograms and do not get selected as carotid.
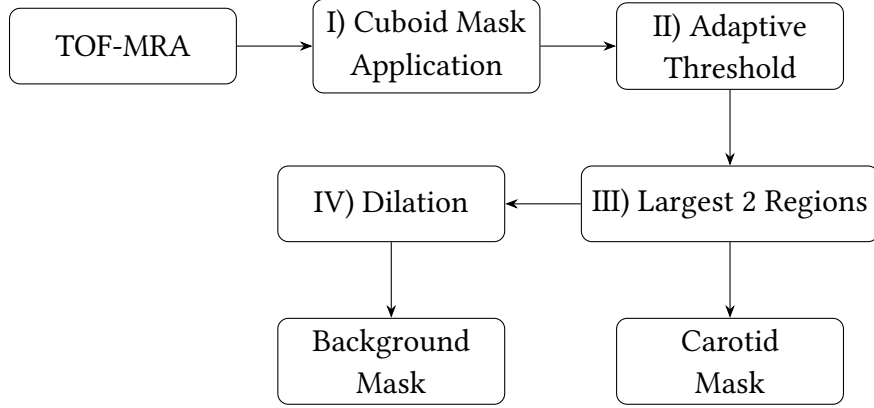
Figure 2.1: Carotid and background mask segmentation pipeline

2.3 Partial Volume Correction

2.3.1 Geometric Transfer Matrix

Direct quantification with the IDIF extracted from the MRI mask of the carotid is impractical due to the strong Partial Volume Effects (PVE) in PET images. This however can be corrected by the use of the Geometric Transfer Matrix (GTM) method [16]. This method considers the observered TAC to be the linear combination of the true real value and the other effecting regions. Here we define two regions, the carotid and the surrounding tissues (background). A mask for extracting the activities of the latter was obtained by dilating the carotid mask by 5 pixels and subtracting the voxels corresponding to the carotid mask (Figure 2.1, Step IV).

$$\underbrace{\begin{bmatrix} T_c \\ T_{bg} \end{bmatrix}}_{\text{Observered}} = \underbrace{\begin{bmatrix} \omega_{c \to c} & \omega_{bg \to c} \\ \omega_{c \to bg} & \omega_{bg \to bg} \end{bmatrix}}_{\text{GTM}} \cdot \underbrace{\begin{bmatrix} T_{IF} \\ T_{tissue} \end{bmatrix}}_{\text{Unknown}}, \tag{2.1}$$

where $\omega_{n \to m}$ are the spill-in and spill-over coefficient of region n onto region m, which is obtained by convolving the binary mask of region n with the system's point spread function and integrating the resulting intensity over region m, normalized by the total signal in region m. where

$$\omega_{n \to m} = \frac{\int_{\Omega_m} \big(h * \chi_n\big)(r)\, dr}{\int_{\Omega_m} \big(h * \chi_m\big)(r)\, dr}, \tag{2.2}$$

with χ_n and χ_m denoting the binary masks of regions n and m, respectively, h the system's point spread function, and Ω_m the spatial domain of region m.

T_c and T_{bg} are respectively the observed carotid and background TACs and T_{IF} and T_{tissue} are the real unknown TACs of the carotid (the input function) and the background tissue.

By inversing the GTM, this system of equations can be easily solved. However, the GTM being a low rank matrix makes the inversion sensitive to noise and biased on small regions such as the carotid [5, 18].

2.3.2 Bayesian Geometric Transfer Matrix

To overcome challenges posed to GTM method, we utilized a Bayesian framework that jointly estimates the input function and tissue kinetics [15]. For each subject, T_{IF} is modeled as a linear combination of a population mean and its principal components. These components are derived by performing principal component analysis (PCA) on a set of AIFs collected from the population. Specifically, for each subject, a subset of 10 random subjects is selected from the dataset—excluding the subject under study—to construct the PCA model.

$$T_{IF}(t) = \mu(t) + \theta_1 v_1(t) + \theta_2 v_2(t) + \theta_3 v_3(t), \tag{2.3}$$

where $\mu(t)$ is the population mean AIF, $v_i(t)$ are the principal components obtained from PCA, and θ_i are the subject-specific weighting coefficients.

The background TAC is then generated by convolving this modeled input function with an impulse response function (IRF) defined by a two-tissue compartment model [19].

$$T_{bg}(t) = T_{IF}(t) \circledast IRF(t; K_1, k_2, k_3), \tag{2.4}$$

where K_1, k_2, and k_3 are kinetic parameters of the two-tissue compartment and IRF is

$$IRF(t) = a_0 e^{-(k_2+k_3)t} + a_1 \text{ with } a_0 = \frac{K_1 k_2}{k_2 + k_3}, a_1 = \frac{K_1 k_3}{k_2 + k_3}. \tag{2.5}$$

Parameter estimation is performed using a Metropolis-within-Gibbs Markov Chain Monte Carlo (MCMC) sampler, which explores the posterior distribution of both the kinetic parameters and the PCA coefficients. In the Bayesian framework [15], all model parameters are collected into the vector Θ. The posterior distribution of Θ given the observed data $\mathcal{D}$ is expressed as

$$p(\Theta \mid \mathcal{D}) \propto p(\mathcal{D} \mid \Theta)\pi(\Theta), \tag{2.6}$$

where $p(\mathcal{D} \mid \Theta)$ is the likelihood function and $\pi(\Theta)$ is the prior distribution over the parameters $\Theta = (\theta_1, \theta_2, \theta_3, K_1, k_2, k_3)$. The maximum a posteriori (MAP) estimate of Θ is given by:

$$\hat{\Theta} = \arg\max_{\Theta} \{\ln p(\mathcal{D} \mid \Theta) + \ln \pi(\Theta)\}. \tag{2.7}$$

2.4 Evaluation

2.4.1 IF Curves

The performance of the proposed IDIF estimation was first evaluated by computing the mean absolute error (MAE) between the cumulative area under the curve (cAUC) of the estimated IDIF and the *ground true* AIF. cAUC was considered to be a more suitable metric since it provides an integrated measure of tracer exposure over time and is less sensitive to local fluctuations or noise in the curve compared to the directly comparing the TACs.

$$\text{cAUC}(t) = \int_0^t IF(\tau)\,d\tau, \tag{2.8}$$

where IF is the input function.

2.4.2 Quantification

However, because the cAUC error does not fully capture the impact of IDIF deviations on kinetic parameters, absolute quantification was also performed to evaluate the performance of the estimated IDIF against the gold standard AIF. This was achieved by utilzing an irreversible two-tissue compartment model (2TCM) via non-linear fitting with the `fitk3` program from the TPCCLIB library developed at the Turku PET Centre [20]—applying the model fitting once with the IDIF and once with the AIF as the input function.

The brain was segmented into regions of interest (ROI) based on the Hammersmith brain atlas [21], and TACs were generated by averaging voxels over each ROI at every time point. The regional influx rate (K_i) was then calculated, from which the corresponding MR_{glu} values were derived.

The mean absolute percentage error (MAPE) of the MR_{glu} in each ROI was calculated and then averaged across the entire dataset:

$$\text{Average MAPE}(\text{MR}_{\text{glu}}) = \frac{100\%}{N} \sum_{i=1}^{N} \left(\frac{1}{N_{\text{ROI}}} \sum_{j=1}^{N_{\text{ROI}}} \left| \frac{\text{MR}_{\text{glu},ij}^{\text{IDIF}} - \text{MR}_{\text{glu},ij}^{\text{AIF}}}{\text{MR}_{\text{glu},ij}^{\text{AIF}}} \right| \right), \tag{2.9}$$

where N is the number of subjects.

Additionally, linear least-squares regression was performed between the regional MR_{glu} obtained by quantification with using AIF and IDIF for each subject. The coefficient of determination (R^2) and the regression slope (S) were obtained for each subject. The mean absolute errors of these metrics across the dataset are given by

$$\text{MAE}(R^2) = \frac{1}{N} \sum_{i=1}^{N} \left| R_i^2 - 1 \right| \tag{2.10}$$

and

$$\text{MAE}(S) = \frac{1}{N} \sum_{i=1}^{N} \left| S_i - 1 \right|, \tag{2.11}$$

where N is the number of subjects and R_i^2 and S_i denote the coefficient of determination and the regression slope for subject i, respectively.

2.5   Implementation

The code was primarily implemented in Python, with some auxiliary components in Bash scripts. The underlying algorithm and implementation was originally developed by Irace et al. [15]. Building on this foundation, a number of improvements and additions were introduced to the code and the algorithm.

In the original carotid segmentation algorithm, the TOF-MRA image was smoothed to reduce noise. The purpose of this smoothing step was to attenuate noise; however, because carotids inherently exhibit high-frequency spatial features, the smoothing inadvertently blurred these critical details, ultimately reducing the accuracy of the segmentation. Hence, this step was removed.

In the adaptive thresholding step, all voxels, including those with zero intensity were originally included. This led to a significant imbalance in the intensity histograms, making the thresholding highly susceptible to variations in the number of slices and the effects of zero padding in the TOF-MRA image. Limiting to only nonzero voxels resulted in an immediate improvement in the final segmentation. Despite these improvements, some non-carotid tissues were inadvertently selected by the algorithm, hence the cuboid mask mentioned in Section 2.2 was introduced.

Furthermore, the code was revised to enhance both implementation and performance. Improvements include major bug fixes, pipeline streamlining, multi-processing support, and the integration of evaluation metrics for both individual subjects and overall dataset performance.

Results

3.1 Carotid Segmentation from MRA-TOF

The measures described in Section 2.2 significantly improved carotid segmentation by effectively excluding brain lesions and undesired venous structures. As illustrated in Figure 3.1, the cuboid mask plays a crucial role in this process. Because no ground truth segmentation is available, visual inspection was used to evaluate the results, which showed that lesions and venous structures were rarely selected by the algorithm. However, the algorithm acted overly conservative at times. It inadvertently excluded the periphery of the larger vessels or completely excluded the narrow ones.


(a) (b)
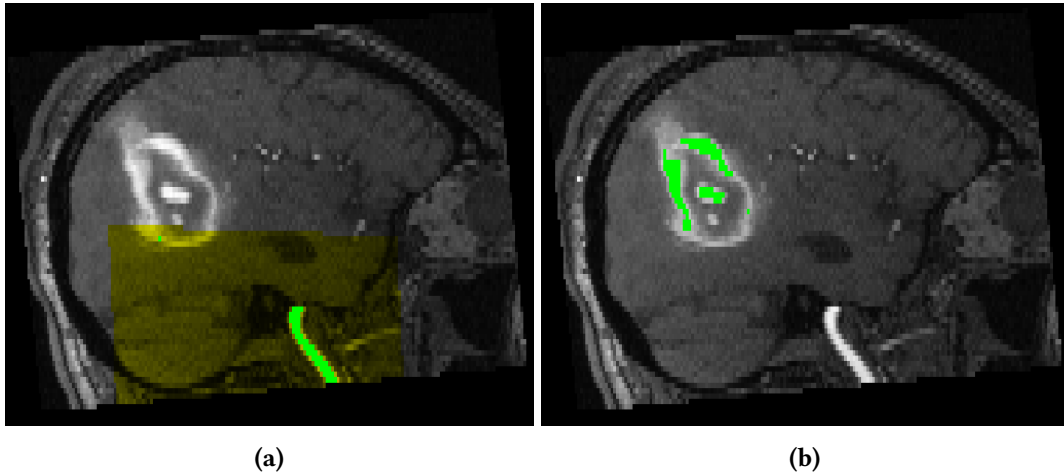
Figure 3.1: Comparison of carotid segmentation (green) with (a) and without (b) a cuboid mask (yellow). In the absence of the cuboid mask, the segmentation algorithm fails to capture the carotid and instead incorrectly identifies the brain lesion

3.2 IDIF

IDIF estimation was performed using both the Bayesian GTM (BGTM) and conventional GTM PVC methods. Figure 3.2 compares the two methods for one of the best- and worst-performing subjects. In the well-performing subject, BGTM significantly outperforms GTM

(MR$_{\text{glu}}$ MAPE of 3.1% vs. 20.9%); however, in the poorly performing case, BGTM falls short of GTM (MR$_{\text{glu}}$ MAPE of 31.4% vs. 19.5%). The average mean absolute error of the cAUC curves across the dataset was 14,202 for BGTM and 33,764 for GTM (Figure 3.3b).
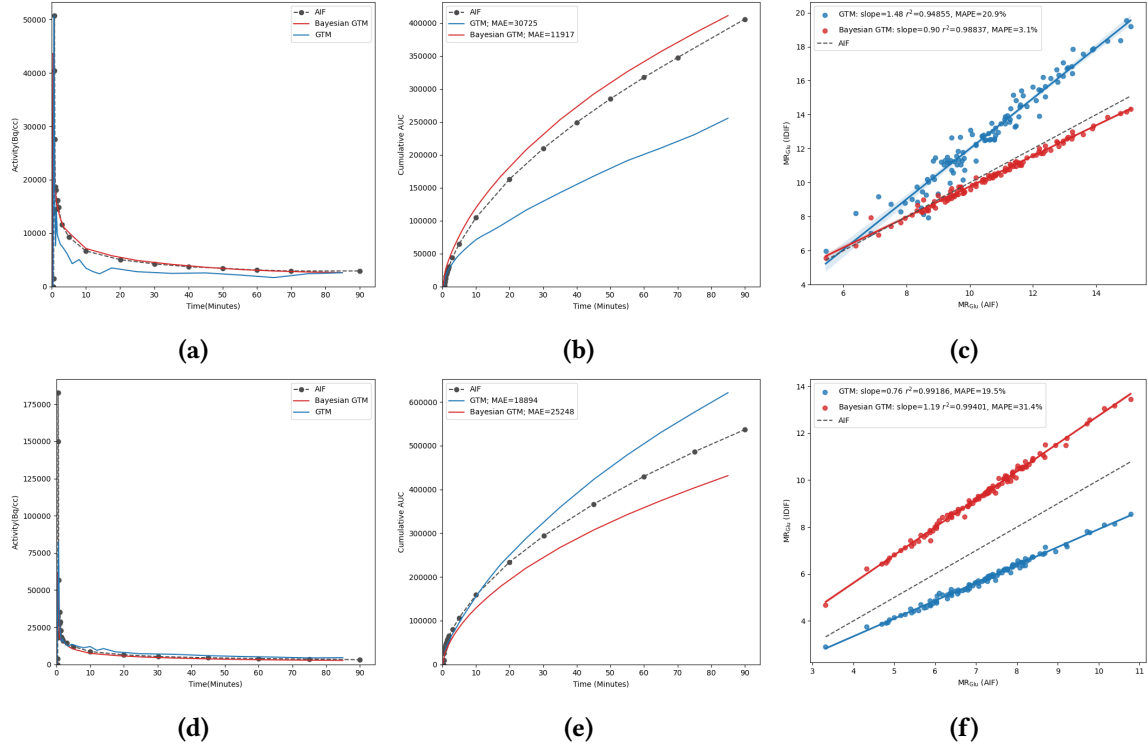

Figure 3.2: Comparison of the IFs (a,d), cumulative AUC curves (b,e), and MR$_{\text{glu}}$ regression lines (c,f) for one of the best-(top row) and worst-performingr(bottom row) subjects

ROI-based quantification was carried out using both IDIF methods, with BGTM yielding significantly better performance. Specifically, the BGTM and GTM methods achieved an average MR$_{\text{glu}}$ mean absolute percentage error (MAPE) of 14.1% and 33%, respectively (Figure 3.3a), and an average MR$_{\text{glu}}$ MAE of 1.42 and 3.5. In addition, the MAE for the coefficient of determination (R^2) and the regression slope (S) were 0.004 and 0.14 for BGTM, compared to 0.030 and 0.304 for GTM, respectively.

A paired t-test was conducted to compare the performance of BGTM and GTM across

Metric	BGTM		GTM		Paired T-Test	
	μ	σ	μ	σ	T-Value	P-Value
IF cAUC MAE	14,202	9,190	33,764	21,212	7.44	7.2×10^{-10}
MR$_{\text{glu}}$ MAPE (%)	14.1	10.1	33.0	31.5	4.32	6.5×10^{-5}
MR$_{\text{glu}}$ MAE	1.42	1.07	3.50	3.38	4.41	4.8×10^{-5}
MR$_{\text{glu}}$ R^2 MAE	0.004	0.006	0.030	0.132	1.45	1.5×10^{-1}
MR$_{\text{glu}}$ Slope MAE	0.14	0.109	0.304	0.230	4.73	1.6×10^{-5}

Table 3.1: Summary of performance metrics for BGTM and GTM methods and their paired t-test.

(a) MR_{glu} MAPE Boxplot
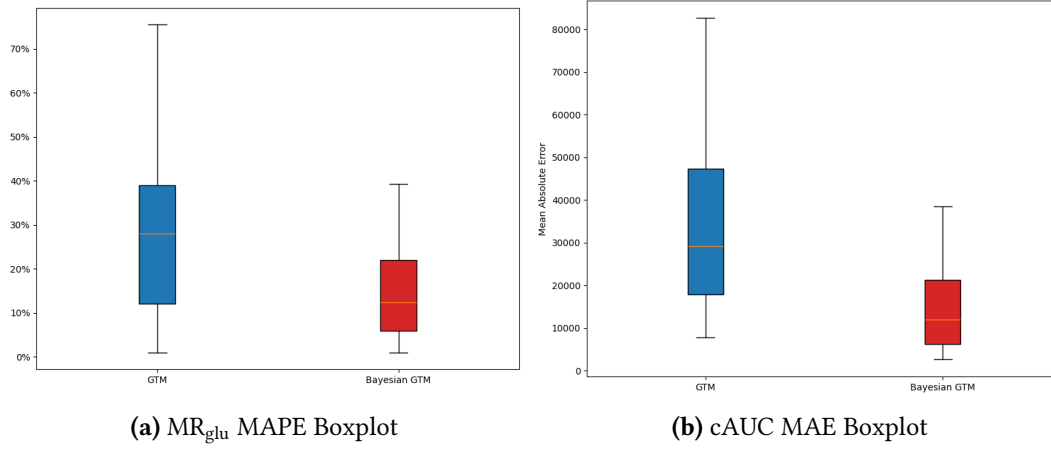
(b) cAUC MAE Boxplot

Figure 3.3: Boxplot of curve and quantification errors

previously mentioned metrics. The results, summarized in Table 3.1, indicate that BGTM significantly outperforms GTM in cAUC MAE($t = 7.44$, $p = 7.2 \times 10^{-10}$), MR_{glu} MAPE ($t = 4.32$, $p = 6.5 \times 10^{-5}$), MR_{glu} MAE ($t = 4.41$, $p = 4.8 \times 10^{-5}$), and MR_{glu} Slope MAE ($t = 4.73$, $p = 1.6 \times 10^{-5}$), demonstrating the effectiveness of the proposed method. However, no significant difference was observed in MR_{glu} R^2 MAE ($t = 1.45$, $p = 0.15$).

As illustrated in Figure 3.4, there is a strong correlation between the cAUC MAE and the quantification errors suggesting cAUC as a reliable intermediate metric.

(a) GTM
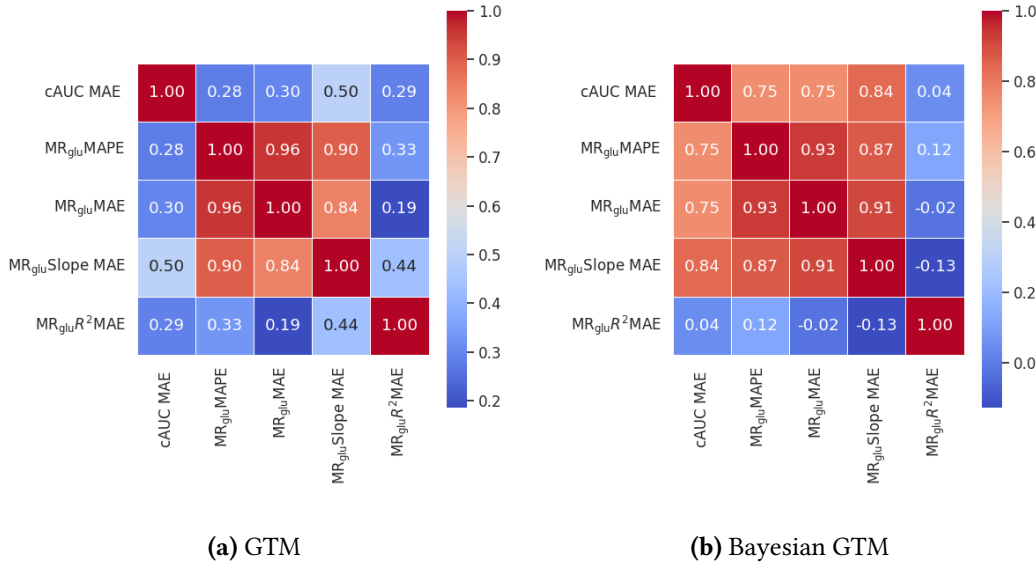
(b) Bayesian GTM

Figure 3.4: Correlation matrix of different metrics for Bayesian GTM and GTM methods

Discussion

The Bayesian Geometric Transfer Matrix (BGTM) method demonstrated significant improvements in IDIF accuracy compared to classical GTM approaches through enhanced handling of partial volume effects. This advancement was achieved by integrating TOF-MRA-guided carotid segmentation with population-based AIF prior knowledge within a Bayesian framework.

The refined segmentation algorithm, particularly through implementation of the cuboid mask, proved crucial for processing challenging data from comatose patients who frequently present brain lesions (Figure 3.1). However, occasional over-conservatism in vessel selection suggests the region-growing and thresholding parameters can be optimized to accurately capture the complete carotid structure. The lack of reference or ground truth carotid mask prevented the evaluation of the segmentation. This also disabled us from accurately evaluating the proposed IDIF algorithm, as the calculated errors are accumulated with the segmentation error as well. With labeled data, deep learning approaches such as U-Net can also be explored to improve segmentation accuracy [22].

The cAUC error reduction (Figure 3.3b) confirms Bayesian priors effectively constrain AIF estimates to physiological ranges. The strong correlation between cAUC errors and quantification errors (Figure 3.4) validates cAUC as a robust intermediate metric for IDIF assessment, enabling rapid validation without requiring full kinetic modeling.

Quantitative analysis revealed strong agreement between BGTM and AIF-derived MR_{glu} values, with the Bayesian approach achieving a 57% reduction in absolute error compared to conventional GTM methods (Table 3.1). Despite this improvement, the observed MAPE results exhibited substantial dispersion (Coefficient of Variation = 71%). This inconsistency is particularly evident in outlier cases where BGTM underperformed (Figure 3.2). Although, further investigation is required to fully characterize the underlying causes, one plausible factor could be TOF-MRA/PET misregistration resulting in inaccurate TAC extraction.

Our analysis was limited to a comatose patient cohort from a single imaging center, which may limit generalizability to populations with normal cerebral blood flow. Future validation should incorporate multi-center studies involving both healthy subjects and different radiotracers to establish broader applicability.

Additionally, the current PCA implementation of randomly selecting 10 subjects from the population lacks practical viability for standardized implementation. Future iterations should only be limited to a predefined population.

Conclusion

This study demonstrates that combining TOF-MRA-guided carotid segmentation with partial volume correction in a bayesian framework improves image derived input function estimation. While the method showed significant improvement in IDIF estimation accuracy, variability in accuracy underscores the challenges posed in artery segmentation as well as partial volume correction. Future validation must address limitations in the current PCA framework by establishing predefined reference cohorts and expanding to multicenter studies with diverse patient populations. By refining anatomical alignment protocols and ensuring consistent prior knowledge integration, this approach can enhance reliability for clinical translation, ultimately supporting safer, patient-friendly quantitative PET imaging.

References

[1] John W Keyes. "SUV: standard uptake or silly useless value?" In: *Journal of Nuclear Medicine* 36.10 (1995), pp. 1836–1839.

[2] Jean Logan et al. "Graphical analysis of reversible radioligand binding from time—activity measurements applied to [N-11C-methyl]-(-)-cocaine PET studies in human subjects". In: *Journal of Cerebral Blood Flow & Metabolism* 10.5 (1990), pp. 740–747.

[3] Clifford S Patlak, Ronald G Blasberg, and Joseph D Fenstermacher. "Graphical evaluation of blood-to-brain transfer constants from multiple-time uptake data". In: *Journal of Cerebral Blood Flow & Metabolism* 3.1 (1983), pp. 1–7.

[4] K Schmidt et al. "Errors introduced by tissue heterogeneity in estimation of local cerebral glucose utilization with current kinetic models of the [18F] fluorodeoxyglucose method". In: *Journal of Cerebral Blood Flow & Metabolism* 12.5 (1992), pp. 823–834.

[5] Paolo Zanotti-Fregonara et al. "Image-derived input function for brain PET studies: many challenges and few opportunities". In: *Journal of Cerebral Blood Flow & Metabolism* 31.10 (2011), pp. 1986–1998.

[6] Jurgen EM Mourik et al. "Image-derived input functions for PET brain studies". In: *European journal of nuclear medicine and molecular imaging* 36 (2009), pp. 463–471.

[7] Chul Hyoung Lyoo et al. "Image-derived input function derived from a supervised clustering algorithm: methodology and validation in a clinical protocol using [11C](R)-rolipram". In: *PLoS One* 9.2 (2014), e89101.

[8] Rugved Chavan et al. "An end-to-end deep learning pipeline to derive blood input with partial volume corrections for automated parametric brain PET mapping". In: *Biomedical Physics & Engineering Express* 10.5 (2024), p. 055028.

[9] Matteo Ferrante et al. "Physically informed deep neural networks for metabolite-corrected plasma input function estimation in dynamic PET imaging". In: *Computer methods and programs in biomedicine* 256 (2024), p. 108375.

[10] Praveen Dassanayake et al. "caliPER: a software for blood-free parametric Patlak mapping using PET/MRI input function". In: *Neuroimage* 256 (2022), p. 119261.

References

[11] Hasan Sari et al. "Estimation of an image derived input function with MR-defined carotid arteries in FDG-PET human studies using a novel partial volume correction method". In: *Journal of Cerebral Blood Flow & Metabolism* 37.4 (2017), pp. 1398–1409.

[12] Thies H Jochimsen et al. "Fully automated calculation of image-derived input function in simultaneous PET/MRI in a sheep model". In: *EJNMMI physics* 3 (2016), pp. 1–17.

[13] Mohammad Mehdi Khalighi et al. "Image-derived input function estimation on a TOF-enabled PET/MR for cerebral blood flow mapping". In: *Journal of Cerebral Blood Flow & Metabolism* 38.1 (2018), pp. 126–135.

[14] Lalith KS Sundar et al. "Towards quantitative [18F] FDG-PET/MRI of the brain: automated MR-driven calculation of an image-derived input function for the non-invasive determination of cerebral glucose metabolic rates". In: *Journal of Cerebral Blood Flow & Metabolism* 39.8 (2019), pp. 1516–1530.

[15] Zacharie Irace et al. "Bayesian partial volume correction for image derived input function". In: *Journal of Cerebral Blood Flow and Metabolism.* Vol. 41. 1_ SUPPL. SAGE PUBLICATIONS INC. 2021, pp. 229–229.

[16] Olivier G Rousset, Yilong Ma, and Alan C Evans. "Correction for partial volume effects in PET: principle and validation". In: *Journal of nuclear medicine* 39.5 (1998), pp. 904–911.

[17] Mark Jenkinson et al. "Fsl". In: *Neuroimage* 62.2 (2012), pp. 782–790.

[18] Ronald Boellaard et al. "Effects of noise, image resolution, and ROI definition on the accuracy of standard uptake values: a simulation study". In: *Journal of Nuclear Medicine* 45.9 (2004), pp. 1519–1527.

[19] Camille Jouvie. "Estimation de la fonction d'entrée en tomographie par é mission de positons dynamique : application au fluorodesoxyglucose". Theses. Université Paris Sud - Paris XI, Dec. 2013.

[20] Vesa Oikonen et al. *TPCCLIB.* Version 0.6.20. Retrieved on 2nd February 2025. Turku PET Centre, University of Turku, 2018. URL: https://gitlab.utu.fi/vesoik/tpcclib.

[21] Alexander Hammers et al. "Three-dimensional maximum probability atlas of the human brain, with particular reference to the temporal lobe". en. In: *Hum. Brain Mapp.* 19.4 (Aug. 2003), pp. 224–247.

[22] Olaf Ronneberger, Philipp Fischer, and Thomas Brox. "U-net: Convolutional networks for biomedical image segmentation". In: *Medical image computing and computer-assisted intervention–MICCAI 2015: 18th international conference, Munich , Germany, October 5-9, 2015, proceedings, part III 18.* Springer. 2015, pp. 234–241.